Continental Shelf Research 110 (2015) 85–99

Contents lists available at ScienceDirect

Continental Shelf Research

journal homepage: www.elsevier.com/locate/csr

Research papers

Mixing and sediment resuspension associated with internal bores in a shallow bay

Eiji Masunaga [a,b,*], Hikaru Homma [a], Hidekatsu Yamazaki [a], Oliver B. Fringer [b], Takeyoshi Nagai [a], Yujiro Kitade [a], Akio Okayasu [a]

[a] Department of Ocean Sciences, Tokyo University of Marine Science and Technology, Tokyo, Japan
[b] Department of Civil and Environmental Engineering, Stanford University, Stanford, USA

ARTICLE INFO

Article history:
Received 29 April 2015
Received in revised form
17 August 2015
Accepted 29 September 2015
Available online 13 October 2015

Keywords:
Internal bores
Internal tides
Nonlinear internal waves
Sediment resuspension
Turbulent mixing

ABSTRACT

Observations of the run-up of internal bores in a shallow bay were made with a tow-yo instrument and mooring arrays with high spatial and temporal resolution. Shoreward propagating internal bores have been studied with laboratory experiments and numerical models, but few observational studies have shown the detailed structure of the run-up of internal bores induced by internal tides. Our observations showed that internal bores propagate along the slope, accompanied by strong turbulent mixing and strong sediment resuspension in a shallow bay. The isothermal displacement due to the bores reached 20 m vertically in a water depth of 40 m. Turbidity measurements showed suspended particles transported from the sloping bottom and offshore above the thermocline, forming an intermediate nepheloid layer (INL). At the head of the bore (dense water), a vortex accompanied by strong vertical motion induced strong vertical sediment resuspension and a steep isothermal displacement. The rate of turbulent kinetic energy dissipation reached 10^{-6} W kg^{-1} at the head of the wave. A nonhydrostatic numerical simulation in a two-dimensional domain reproduced fine features associated with the run-up of an internal bore and the vortex motion at its head.

1. Introduction

Shoreward propagating internal waves are ubiquitous features in the coastal ocean (e.g., Fu et al., 1982; Helfrich and Melville, 2006; Bourgault et al., 2007; Nam and Send, 2011; Walter et al., 2012). These waves run-up on a slope and break, producing what are typically referred to as "boluses" or "bores" (Wallace and Wilkinson, 1988; Helfrich, 1992). Shoreward propagating internal bores have been investigated in both numerical simulations (e.g., Venayagamoorthy and Fringer, 2006) and observations (e.g., Walter et al., 2012) and are hypothesized to be important drivers of cross-shelf transport of nutrients (e.g., Leichter et al., 1996), sediment (e.g., McPhee-Shaw, 2006), and zooplanktons and larvae (e.g., Pineda, 1994). An internal bore generates a vortex core accompanied by strong vertical motion at its head (Venayagamoorthy and Fringer, 2006). The vortex structure of internal bores has been observed with high-resolution thermistor arrays on a sloping continental shelf (Hosegood et al., 2004; Van Haren, 2009).

Isopycnal displacements induced by internal tides can be amplitudes of roughly 20–80 m on continental shelves (Huthnance, 1989; Petruncio et al., 1998). In submarine canyons, previous studies pointed out large isopycnal displacements of 60–120 m due to internal tides (Broenkow and McKain, 1972; Shea and Broenkow, 1982; Wang et al., 2008). Broenkow and McKain (1972) observed an internal tide with an isopycnal displacement of 80 m in a depth of 120 m. Strong horizontal currents in bottom boundary layers are also generated by internal waves (e.g., Wang et al., 2008; Van Gastel et al., 2009). Van Gastel et al. (2009) observed internal bores accompanied by strong currents reaching 1.0 m s^{-1}.

Internal tides, or internal waves of tidal frequency, are generated at critical topography where the topographic slope matches the internal wave beam angle (Vlasenko et al., 2005; Van Gastel et al., 2009). In the presence of critical slopes, internal wave reflections lead to strong energy convergence over continental shelves (e.g., Thorpe, 1998; Cacchione et al., 2002). Ivey et al. (2000) estimated that when internal waves reflect on a critical slope, the turbulent kinetic energy dissipation rate reaches $O(10^{-6})$ W kg^{-1}. The appearance of internal bores is intermittent and is typically not associated with any particular tidal frequency (Hosegood et al., 2004; Van Haren, 2009). However, Vlasenko et al. (2012) was able to compute a lag time between the appearance of internal bores and the semidiurnal barotropic tide that was

* Correspondence to: Department of Ocean Sciences, Tokyo University of Marine Science and Technology, 4-5-7 Konan, Minato-ku, Tokyo, Japan.
E-mail address: emasun0@kaiyodai.ac.jp (E. Masunaga).

http://dx.doi.org/10.1016/j.csr.2015.09.022
0278-4343/

consistent with the wave propagation time between the hypothesized wave generation site and the observation site.

Klymak and Moum (2003) and Carter et al. (2005) observed strong turbulent mixing in internal solitary waves (boluses) advancing on a sloping shelf. Venayagamoorthy and Fringer (2006) and Vlasenko and Hutter (2002) simulated fine-scale breaking processes of boluses using numerical models. Masunaga et al. (2015) reported that such internal wave breaking events can significantly contribute to river plume mixing near the sea surface. The passage of internal bores provides a burst of strong turbulent kinetic energy along the slope (Boegman and Ivey, 2009; Venayagamoorthy and Fringer, 2006). Walter et al. (2012) showed that internal bores generate high-frequency temperature fluctuations associated with strong turbulent mixing. Such high-frequency temperature fluctuations in large-scale internal waves have been observed by Antenucci and Imberger (2001) and Boegman et al. (2003) who hypothesized that the high-frequency motions arise from a shear instability.

In addition to strong turbulent mixing, internal bores induce strong sediment resuspension (e.g., Cacchione et al., 2002; McPhee-Shaw and Kunze, 2002). Hosegood et al. (2004) and Bonnin et al. (2006) observed sediment resuspension associated with the passage of bore waves. McPhee-Shaw and Kunze (2002) investigated sediment resuspension and slope angle conditions from tank experiments. They showed that resuspension and the growth of turbidity intrusions into the ocean interior are enhanced near critical slopes. These turbid intrusions, which become detached from boundaries and intrude into the ocean interior, have frequently been observed in coastal areas (Dickson and McCave, 1986; McPhee-Shaw et al., 2004; Nakatsuka et al., 2004) and are referred to as intermediate nepheloid layers (INLs). Lateral dispersal of sediments, nutrients, metals, and organic matter derived from the seabed is much greater than that derived from vertical settling from the ocean surface (Van Weering et al., 2001; Nakatsuka et al., 2004; McPhee-Shaw, 2006). Cross-shelf transport of such material from nearshore areas due to internal waves is vital for biological production in offshore sites (Nakatsuka et al., 2004; McPhee-Shaw, 2006). Cacchione et al. (2002) and Puig et al. (2004) also reported that erosion and resuspension of sediments are enhanced at critical slopes. Furthermore, several studies have shown that the small scale vortex motion associated with internal bores generates strong sediment resuspension (Boegman and Ivey, 2009; Van Haren, 2009; Richards et al., 2013; Masunaga and Yamazaki, 2014). At the head of bores, a strong upward flow and strong turbulent mixing are generated by the vortex motion (Richards et al., 2013; Masunaga and Yamazaki, 2014). However, due to the lack of field obsrvations, physical processes associated with such small-scale vortex motion are not well understood.

Although previous studies have focused on internal bore dynamics, few have revealed the detailed structure of the run-up of internal bores on slopes using in situ surveys. In this paper, we report on observations of detailed features of the run-up of internal bores in Otsuchi Bay, Japan. We deployed a recently developed YODA Profiler (Masunaga and Yamazaki, 2014), which captures data at high spatial resolution. Masunaga and Yamazaki (2014) used the YODA Profiler to reveal detailed structure of river plumes, small-scale internal waves and sediment resuspension. We also deployed a high-resolution temperature mooring array concurrent with the YODA Profiler survey. In addition to the field observations, we used the nonhydrostatic SUNTANS model (Fringer et al., 2006) to further investigate details of the internal bores. Section 2 outlines the instrumentation and field surveys. Section 3 presents an overview of the physical oceanography of the bay and an analysis of the fine bore features that were observed in field surveys and reproduced by the model. Section 4 discusses the vortex motion, sediment resuspension and turbulent mixing due to the internal bores, along with numerical simulation results. Finally, Section 5 presents summary and conclusions.

2. Method

2.1. Location

Field campaigns were carried out in Otsuchi Bay, located on the Sanriku Coast, Iwate Prefecture, Japan (Fig. 1), in September 2012 and 2013. The Sanriku Coast has steep, narrow bays formed by the partial submergence of river valleys; this type of coastline is called

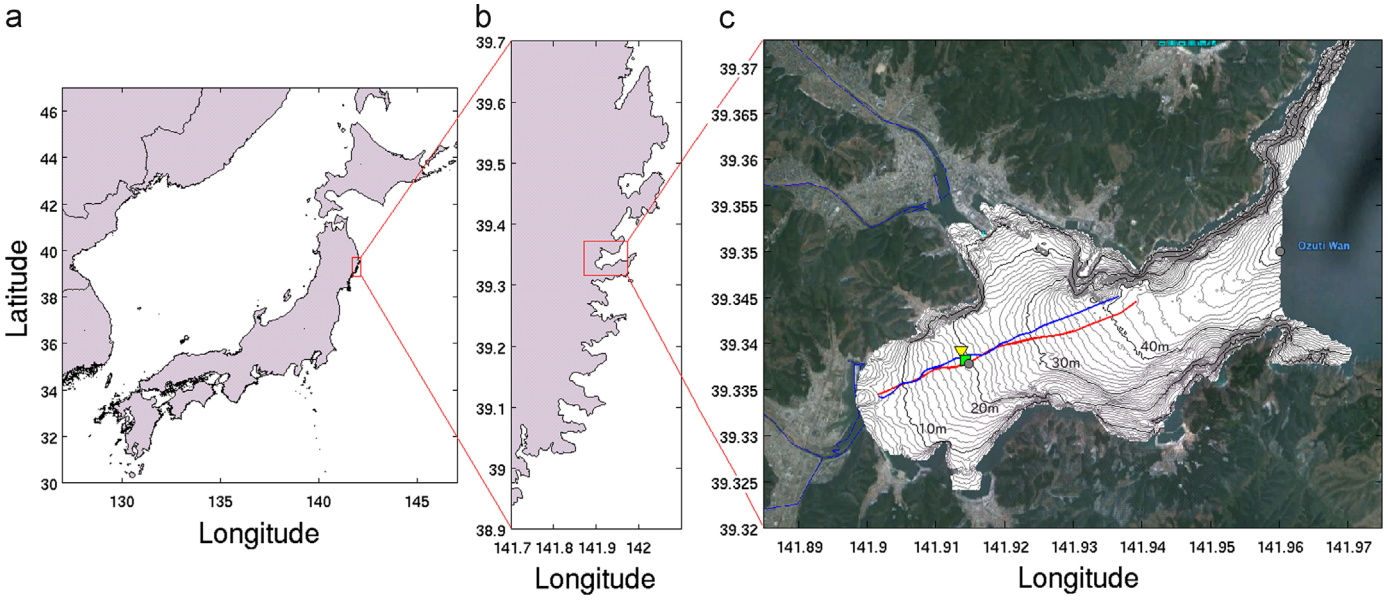

Fig. 1. (Color figure online). Observation area. (a–c) show coastlines around Japan, the Sanriku Coast, and Otsuchi Bay, respectively. The blue and red lines in (c) are transect observation lines on 27 September 2012. The ADCP and the thermistor array mooring sites in 2012 are indicated by the yellow inverted triangle and the light green square. The two mooring sites in 2013 are represented by the gray circles. Black and gray contour lines in (c) indicate isobaths.

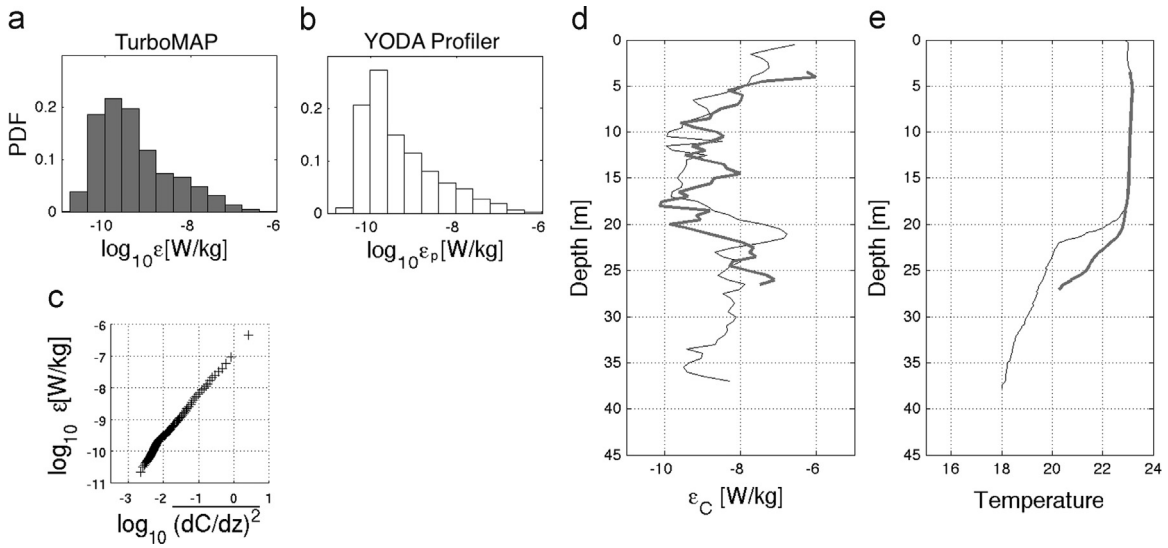

Fig. 2. (a, b) PDFs of ε, (c) QQ plot between ε obtained by TurboMAP-Glider, and the variance of the dC/dz obtained by the YODA Profiler, (d) vertical profiles of ε, and (e) temperature. Thin black and thick gray lines (d) and (e) represent data from the YODA Profiler and TurboMAP-Glider, respectively.

a "ria" (Fig. 1). Otsuchi Bay is a long narrow bay; the length and the width of the bay are 8 km and 3.5 km, respectively. The maximum depth of the observation area is approximately 50 m. The bay has a gently sloping bottom with a slope angle of approximately 0.6 degrees. Three rivers flow into the bay: the Unosumai River, the Otsuchi River, and the Kotsuchi River. The Unosumai river mouth is located at the innermost west part of the bay, and the mouths of the Otsuchi River and the Kotsuchi River are located at the northwest part of the bay (Fig. 1). The total discharge from the rivers ranges between 3 and 35 $m^3 s^{-1}$ (Anbo et al., 2005; Otobe et al., 2009). Okazaki (1990) observed the intermittent appearance of internal bores in Toni Bay, which is located near Otsuchi Bay (17 km south of Otsuchi Bay). The off-Sanriku area is in the Kuroshio–Oyashio transition zone, which is alternately occupied by cold, nutrient-rich Oyashio water and warm, nutrient-depleted Kuroshio water (e.g., Hanawa and Mitsudera, 1986), and is known as a highly productive fishery ground. Okazaki (1994) reported that the fish catch is positively correlated to cold-water intrusion events due to internal tides in Toni Bay (located in the Sanriku Coast).

2.2. Transect observations

Transect observations were carried out using the YODA Profiler (Masunaga and Yamazaki, 2014) and the RiverRay ADCP (Teledyne RD Instruments) on September 27, 2012 and September 11, 2013. The YODA Profiler is a free-fall tow-yo instrument and provides high-resolution measurements of physical structures in shallow coastal areas. To deploy these instruments, we used two fishing boats provided by the Shin-Otsuchi Fishery: the Senshu-maru in 2012 and the Daimutsu-maru in 2013. The transect observation line extends from the Unosumai River mouth (bay head) to the bay mouth, and the distance of observation lines was approximately 3.5 km (Fig. 1). In order to observe high-resolution data horizontally, the ship speed and the sinking speed of the YODA Profiler were adjusted to 2 kts and 0.3 m s^{-1}, respectively. The YODA Profiler is equipped with conductivity–temperature–depth (CTD), fluorescence, turbidity, and dissolved oxygen sensors, and data were collected at 10 Hz. We used data obtained during a stable free-fall descending phase. The horizontal distance between tow-yo profiling points increased from 24 m to 364 m as the depth increased. The YODA Profiler also allows us to estimate the turbulent kinetic energy dissipation rate, ε, from vertical fluctuations of conductivity, dC/dz, making use of the method described in Masunaga and Yamazaki (2014). The RiverRay ADCP collects the data at 1 Hz, and current data were averaged over 1-minute intervals.

2.3. Microstructure observations

The YODA Profiler does not carry a microstructure sensor, and thus we cannot measure the intensity of turbulence directly using this instrument. Masunaga and Yamazaki (2014) developed a statistical method to estimate a proxy of the dissipation rate by making use of conductivity signals. The proxy dissipation rate can be inferred from the variance of the conductivity with the following logic (Masunaga and Yamazaki, 2014):

(1) The dissipation rate of turbulent kinetic energy and temperature gradient follow a joint lognormal probability density function (PDF);
(2) Conductivity signals follow temperature signals;
(3) The dissipation rate of turbulent kinetic energy and conductivity gradient follow a joint lognormal PDF.

We refer to the dissipation inferred from the YODA Profiler as the pseudo-dissipation rate, ε_P, in this study. The estimation of ε_P from the YODA Profiler requires the background PDF of ε from a separate microstructure survey in the same area. Therefore, we collected microstructure data using a glider-type microstructure profiler, TurboMAP-Glider (Foloni-Neto et al., 2014), at numerous points in Otsuchi Bay during 26–27 September, 2012. The TurboMAP-Glider was deployed from the R/V Grand-maillet (the University of Tokyo). In order to infer ε_P from the YODA Profiler, we estimated coefficients a and b from the empirical formula

$$\varepsilon_p = a\left[\overline{(dC/dz)^2}\right]^b \quad (1)$$

with the QQ plot (quantile versus quantile) between ε from the TurboMAP-Glider and ε_P from the the variance of dC/dz from the YODA Profiler (Fig. 2c). Using least-squares regression, $a = 1.42 \times 10^{-7}$ and $b = 1.37$. The PDFs of the dissipation from the two instruments are consistent with each other (Fig. 2a and b). The PDF of ε_P from the YODA Profiler was not significantly different from the PDF obtained from TurboMAP-Glider (Kolmogorov-Smirnov test, $p < 0.1$), and hence the PDFs from the two

Table 1
Instrument deployments and recovery by location, time, and depth.

Instrument	Location		Deployment time (JST)	Recovery time (JST)	Depth
Thermistor array	39°20.352′ N	141°52.824′ E	25 September 2012 13:44	27 September 2012 14:40	20 m
ADCP	39°20.293′ N	141°52.855′ E	25 September 2012 13:31	27 September 2012 14:45	20 m
Thermistor array and ADCP	39°21.007′ N	141°57.610′ E	10 June 2013 8:08	13 September 2013 8:03	54 m
Electromagnetic current meter	39°20.270′ N	141°54.889′ E	10 June 2013 10:06	13 September 2013 8:37	20 m

instruments were statistically identical. Vertical profiles of the dissipation estimated from the YODA Profiler are in reasonable agreement with TurboMAP-Glider data (Fig. 2d and e). We do not claim that ε_P is an accurate estimate of the dissipation, but ε_P should give a reasonable approximation of the dissipation, at least to within the correct order of magnitude (Masunaga and Yamazaki, 2014; Masunaga et al., 2015).

2.4. Mooring observations

A thermistor mooring array and an Acoustic Doppler Current Profiler (ADCP) were placed in the middle of the transect observation line at a depth of approximately 20 m (Fig. 1) during September 25–27, 2012. Table 1 shows the locations of the two mooring sites and the deployment recovery times. The distance between these two moorings was approximately 120 m. HOBO U24 sensors (Onset Computer Corporation) were used as a thermistor array and were arranged from near the bottom to approximately 10 m above the bottom at 0.4-m intervals. The data sampling frequency for the HOBO U24 sensors was set to 0.1 Hz. The MicroCAT C–T sensor (Sea-Bird Electronics, Inc.) and the Compact-CTD (JFE Advantech, Ltd.) were also mounted at 2 m and 1 m above the bottom, respectively. Sampling intervals of the MicroCAT and the Compact-CTD were set to 10 s and 1 min, respectively. The Compact-CTD also carries fluorescence and turbidity sensors. We deployed a 600 kHz four-beam ADCP (Teledyne RD Instruments) mounted on the bottom using a bottom-landing frame. The ADCP was set to resolve 0.5-m vertical bins at 2-second sampling intervals (each sampling includes 8 pings). The ADCP also carries a pressure sensor and a temperature sensor.

For the 2013 campaign, a thermistor mooring array was deployed with a 600 kHz four-beam ADCP (Teledyne RD Instruments) at a deeper site (54-m depth), and an electromagnetic current meter (INFINITY-EM, JFE Advantech Ltd.) was deployed near the bottom at a shallower site (21 m depth) from June to September 2013 (Fig. 1, Table 1). For the deeper mooring, twenty-three TidbiT v2 (Onset Computer Corporation) temperature sensors were equally spaced between 2.5 m above the bottom and 35.5 m above the bottom. The sampling interval of the TidbiT temperature sensors was set to 5 min. The ADCP was set to resolve 1 m vertical bins at 5 min sampling intervals (each sample includes 50 pings). The electromagnetic current meter collected data every 10 min, and the observation mode was set to a burst mode (10 values were collected every 10 min).

2.5. Sediment sampling

We collected bottom sediment samples in the bay using a Smith–MacIntyre Bottom Sampler in September 2012. The laser diffraction particle size analyzer, LS-200 (Beckman Coulter, Inc.), was used to measure the particle size. The LS-200 measures particle density in the size range between 0.375 and 1822 μm. Fig. 3 shows the locations of the bottom sampling points.

2.6. Numerical set up

In order to reproduce the observed internal bores numerically, we used the nonlinear and nonhydrostatic SUNTANS model (Fringer et al., 2006) in a two-dimensional domain that is 10 km long and 80 m deep. The topography in the domain is consistent with the along channel slope in Otsuchi Bay. The horizontal grid spacing, the vertical grid spacing, and the time step are 20 m, 0.56 m, and 1 s, respectively. The Mellor–Yamada 2.5 level turbulent closure model (Mellor and Yamada, 1982) is used with the two-dimensional SUNTANS. The initial conditions for the temperature and the salinity are taken from the transect observations with an initial thermocline depth of 40 m (interface of the internal wave). The model is forced by the horizontal velocity profile of the first-mode internal wave at the ocean boundary to reproduce internal tides originating outside of and propagating into Otsuchi Bay. The frequency of the internal tides is set to the M_2 semidiurnal tidal frequency. In order to reproduce the observed

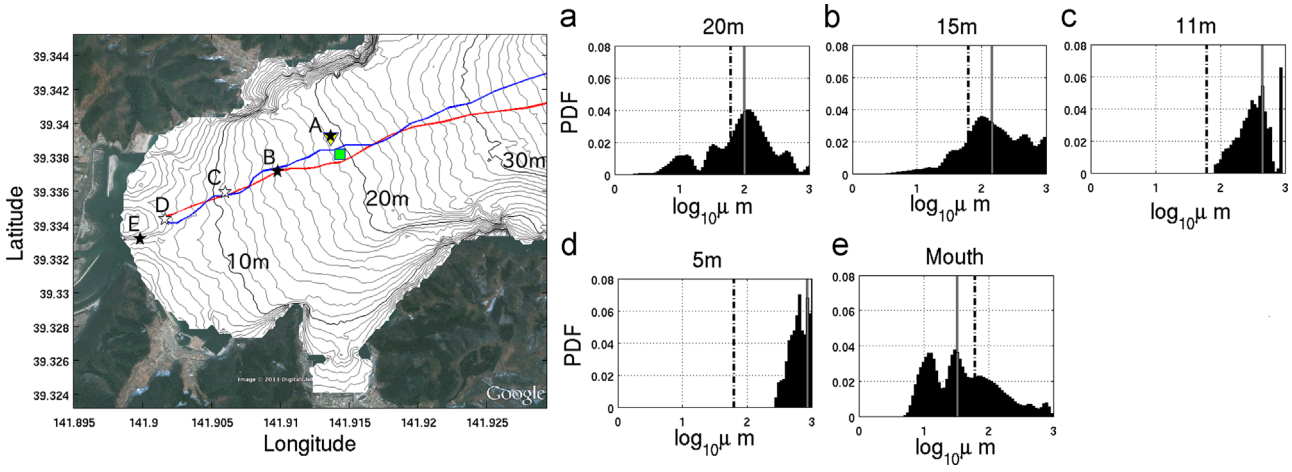

Fig. 3. Bottom sampling locations and grain size distributions of the sediment samples. Stars indicate sampling points (A–E). Histograms (A–E) show the particle size at each sampling point in the left panel. The black dash–dotted line is the threshold between the silt and the sand (62.5 μm), and the gray line marks the median particle size.

internal bores, the maximum velocity amplitude of the internal wave velocity at the boundary is set at 0.2 m s^{-1}. The shallow coast boundary is closed in the domain. We did not employ the heat flux model between the sea surface and the atmosphere, since the time scale of the simulation is too short to be affected by thermally-driven circulation.

3. Results

3.1. Cold water intrusion events

The observed temperature time series at the bottom of the mooring station (Fig. 1c) showed that temperature dropped three times during the 2012 campaign (Fig. 4a, Events 1–3). These cold (dense)-water intrusion events are called "internal bores" (e.g., Wallace and Wilkinson, 1988; Helfrich, 1992; Leichter et al., 1996; Walter et al., 2012). The mooring observational period ended during the last low-temperature intrusion period (Event 3). Thus, observational data did not completely reveal the last low-temperature event. The temperature dropped approximately 1.0, 2.5, and 4.5 °C during Event 1, Event 2, and Event 3, respectively. These events occurred after large-amplitude flood tides. Low-temperature intrusions appeared to be related to the barotropic tide. However, the time intervals between the beginning of the temperature decrease and the lowest tide (beginning of the flood) were different for each event; the intervals were 8.97, 8.68, and 6.45 h for Event 1, Event 2 and Event 3, respectively. Meso-scale currents and coastally-trapped shelf waves modulate the phase speed of internal waves (Vlasenko et al., 2012), it is supposed to be

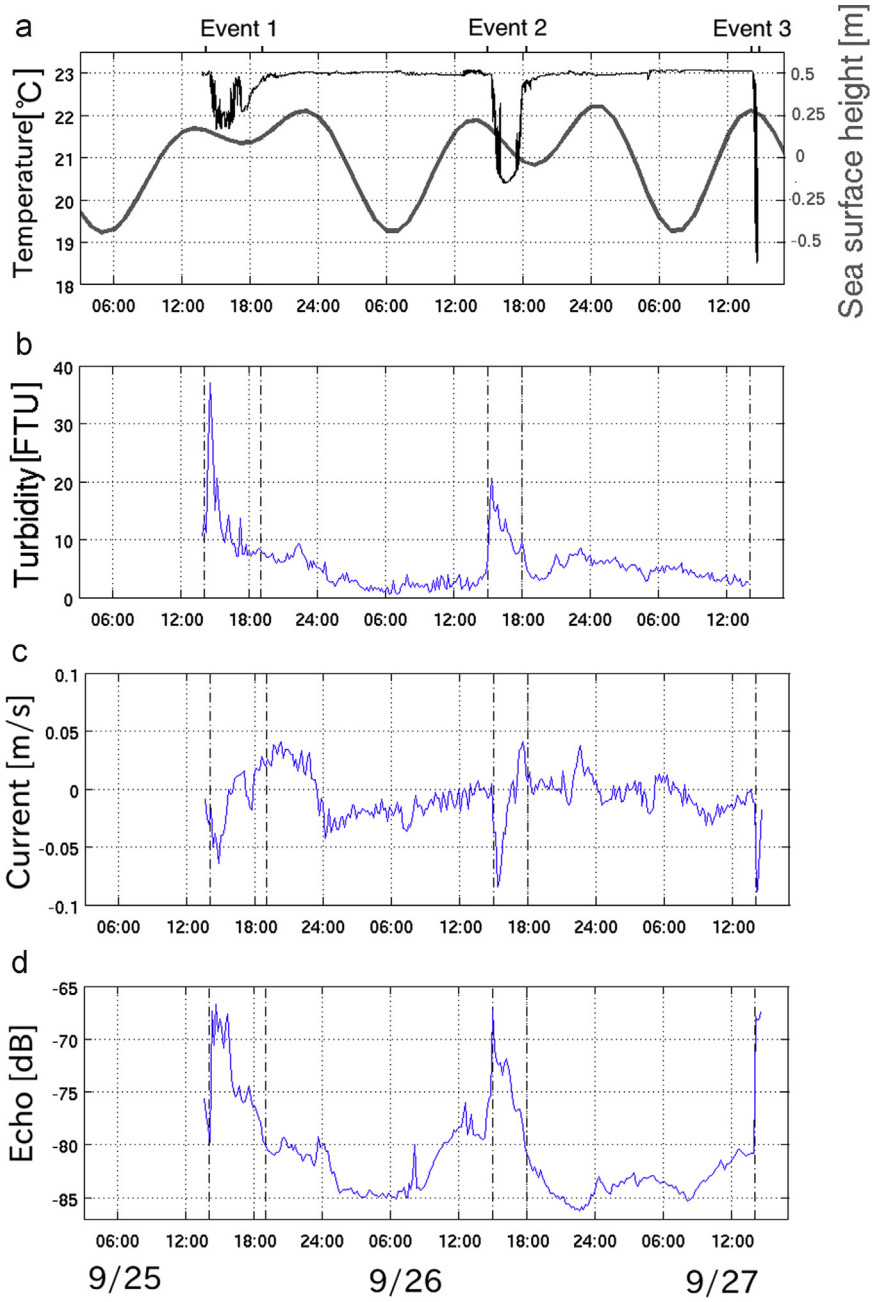

Fig. 4. (a) Bottom water temperature (thin black line) and sea-surface height (thick gray line), (b) turbidity obtained by the Compact-CTD, (c) along-channel currents, and (d) echo intensity [dB] at 2 m above the bottom obtained by ADCP at the mooring site in September 2012. The dash–dotted lines indicate the start and end of the bore events. Positive (negative) values in panel (c) indicate offshore (onshore) flow.

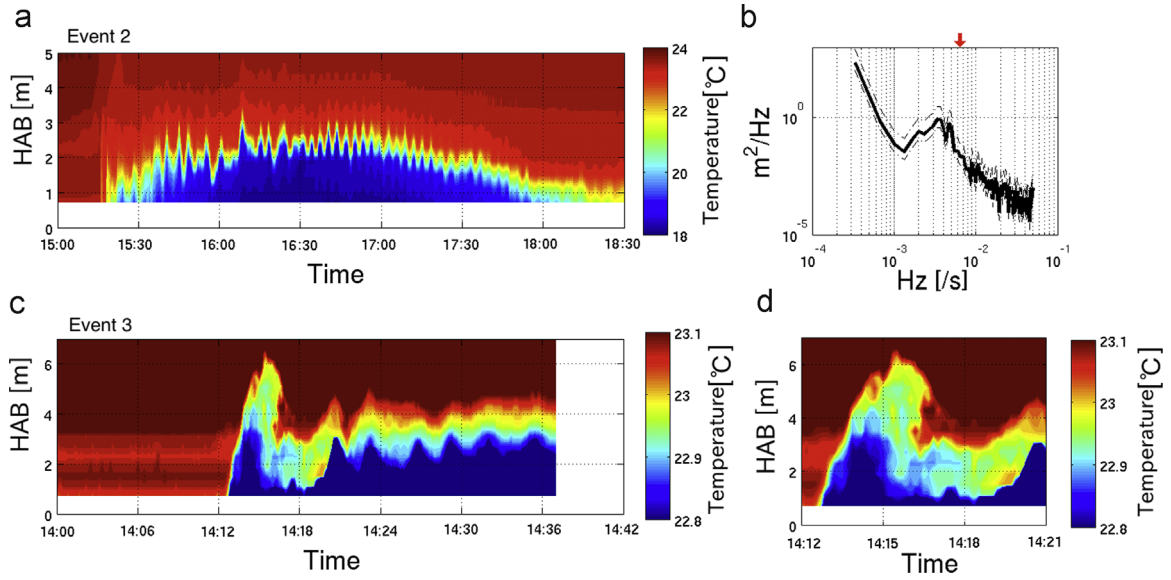

Fig. 5. (Color figure online). (a, c) Temperature distributions during bore wave periods on 26 (Event 2) and 27 (Event 3) September, and (b) spectra of the 22-degree isothermal depth fluctuation shown in (a). (d) is a close-up of the head of the wave shown in (c). The red arrow in (b) indicates the buoyancy frequency in the internal bore wave on September 26, 2013. The dash–dotted lines in (b) indicate a 95% confidence interval of the spectra. Periods of panels (a) and (c) are represented by "Event 2" and "Event 3", respectively, in Fig. 4 a. HAB represents height above the bottom.

difficult to predict the appearance of internal tides in coastal areas.

Temperature observed by the thermistor array showed high-frequency isothermal depth displacements (Fig. 5a) and a vortex-like structure (Fig. 5d). A spectrum of the isotherm fluctuation showed a significant peak between 10^{-3} and 10^{-2} Hz (Fig. 5b); this peak frequency was near the buoyancy frequency, N, in the observed internal bore. Inside the internal bore, N was approximately 5×10^{-3} s^{-1}, where the buoyancy frequency, N, was estimated with

$$N=\sqrt{-\frac{g}{\rho_0}\frac{d\rho}{dz}}, \tag{2}$$

where g is the gravitational acceleration, z is the vertical coordinate with positive upward, ρ is the local density, and ρ_0 is the mean density. Antenucci and Imberger (2001) and Boegman et al. (2003) observed high-frequency internal waves near the buoyancy frequency in internal seiches in lakes. They suggested that these waves resulted from shear instability in large-scale internal waves. However, our observations did not show features related to a shear instability because of the low resolution of the thermistor array. The observed high-frequency isothermal displacement shown in Fig. 5a is likely related to the largest eddy induced by a shear instability. Using a high-resolution numerical model, Walter et al. (2012) showed a vortex structure accompanied by a steep isothermal displacement at the head of the bore (low temperature dense water), which is consistent with the steep displacement that appeared in our observations (Fig. 5c).

Temperature data from the YODA Profiler showed a fine feature in the internal bore accompanied by a low-temperature water mass propagating up slope into shallow water (Fig. 6b and c). Observed data shown in Fig. 6 were obtained during 9:13–10:15 (phase A in Fig. 6b) and 13:16–14:22 (phase B in Fig. 6c) on 27 September 2012 (during Event 3). The isothermal displacement caused by the bore reached 20 m vertically at 40 m depth (Fig. 6b and c). Assuming that the bore front was located at the deepest right edge of the transect line in phase A, and that the bore front propagated approximately 2000 m across the slope between phases A and B (4 h), the average propagation speed of the bore and the average vertical displacement speed of the thermocline were at least 0.14 m s^{-1} and 1.4×10^{-3} m s^{-1}, respectively. In addition to the observations in September 2012, we succeeded in obtaining four clear snapshots of an internal bore running up and receding down the slope in September 2013 (Fig. 7).

The RiverRay ADCP data showed onshore currents (0.1–0.15 m s^{-1}) below the interface of the internal wave (20–30 m) and onshore currents (0.05–0.15 m s^{-1}) in the upper layer (5–20 m); the upper layer flow opposed the lower cold layer flow (Fig. 6i), and is due to first-mode internal waves. This flow is referred as a "sakashio (inverse flow)" by Japanese fishermen and is frequently found in bays along the Sanriku Coast (Okazaki, 1990). Currents in the cold water layer were consistent with the bore wave propagation speed (0.14 m s^{-1}). Although the current near the sea surface (0–5 m) flows in an opposite direction from the subsurface flow, this layer is influenced by the wind stress (Fig. 6h and i). Ten-minute averaged moored ADCP data showed onshore flow near the bottom at the beginning of the wave events (Fig. 4c, 9/25 15:00, 9/26 15:00, 9/27 14:00) and offshore flow during the receding phases (Fig. 4c, 9/25 16:00, 9/26 17:00). Assuming that the barotropic tidal wavelength is long relative to the length of the bay, the magnitude of the barotropic currents in the bay can be calculated from the simple volume conservation equation (Petruncio et al., 1998)

$$u=\frac{\eta A}{thw}, \tag{3}$$

where the tidal range is approximately $\eta=1$ m for the M_2 semi-diurnal tide, A is the surface area of the bay (approx. 10^7 m^2), t is the duration of the flood or ebb tide (6.2 h), h is the average depth across the bay mouth (approx. 50 m), and w is the width of the bay at the mouth (approx. 2000 m). With this formula, the average semi-diurnal barotropic current was approximately 4.5×10^{-3} m s^{-1} in Otsuchi Bay. This barotropic current speed is considerably weaker than the observed currents, and thus the currents were largely dominated by the baroclinic tidal current in Otsuchi Bay during our field campaign.

The salinity distribution observed by the YODA Profiler showed that a thin low salinity layer (within 10 m) spread over the bay due to river discharges from the three rivers flowing into Otsuchi Bay (Fig. 6d and e). As it propagated along the surface as a river plume, the low salinity water from the rivers did not influence the currents

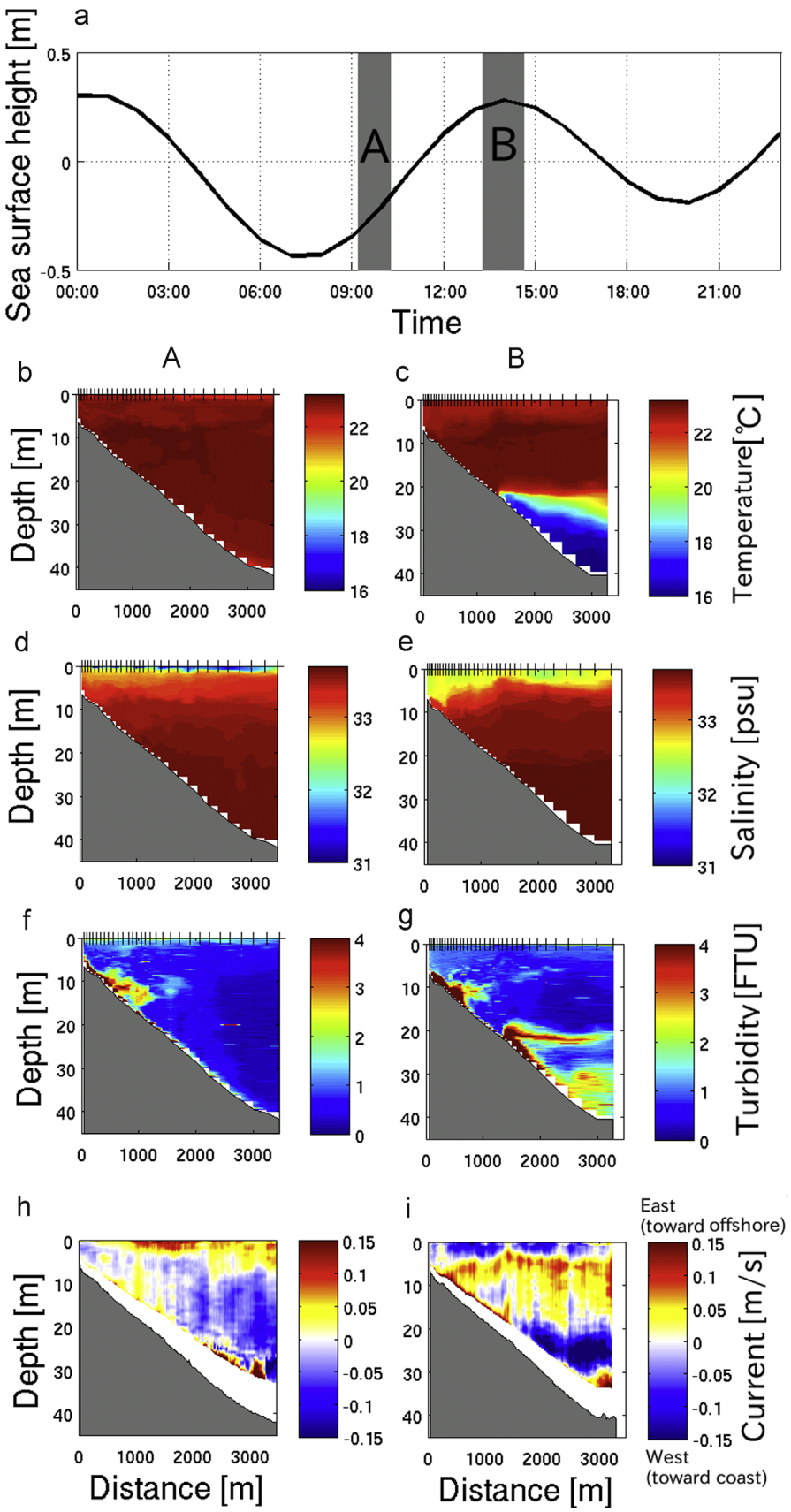

Fig. 6. (a) Tidal elevation observation results obtained by (b–g) YODA Profiler and (h, i) RiverRay ADCP on 27 September 2012 (during Event 3). Shaded areas in (a) indicate transect observation periods: (A) the beginning of the flood tide and (B) the high tide. Observations show (b, c) temperature, (d, e) salinity (f, g) turbidity, and (h, i) east–west current [m s^{-1}] distributions observed (b, d, f) before the bore wave period and (c, e, g) during the bore wave period. Tick marks on the top axis in panels (b–g) indicate the YODA Profiler data collection points.

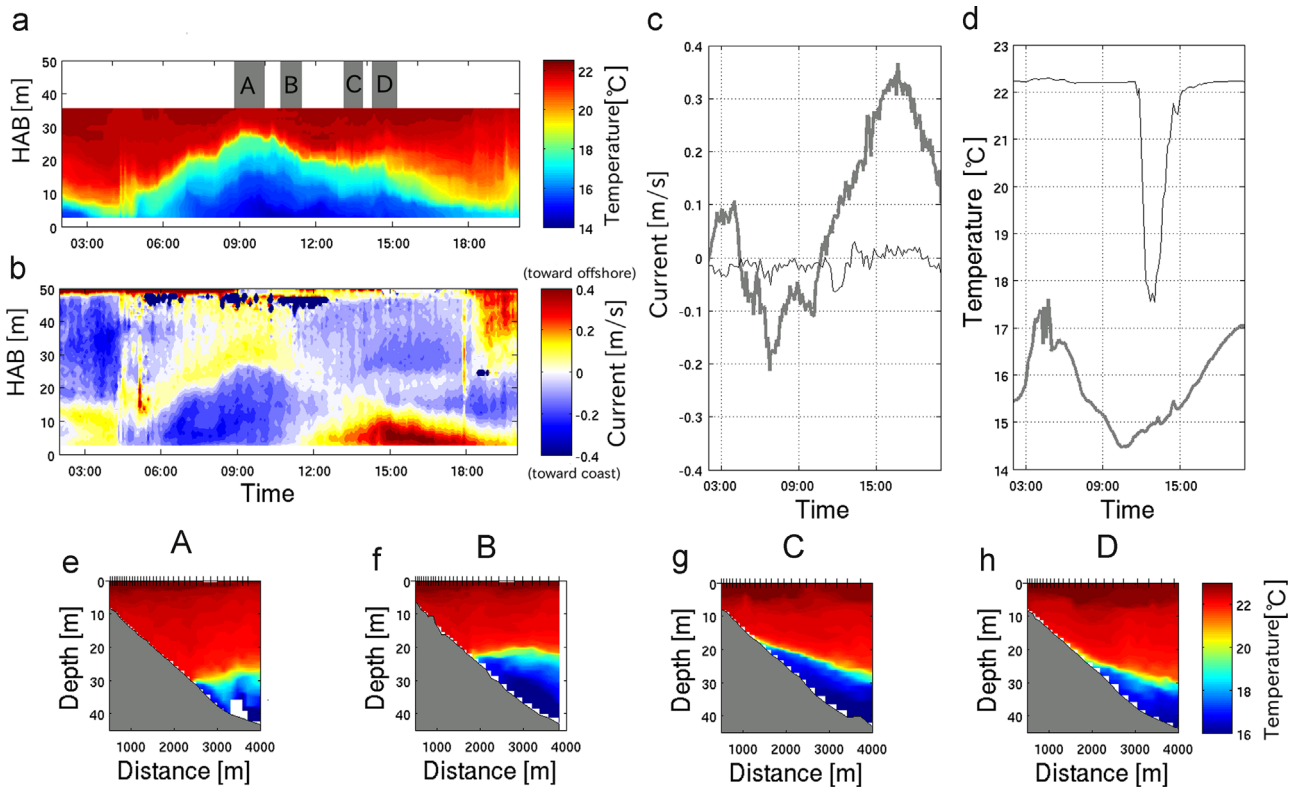

Fig. 7. (Color figure online). (a) Temperature and (b) east–west currents observed from the mooring array, (c) currents and (d) temperature observed near the bottom at the deep mooring site (54 m, thick gray line) and the shallow site (21 m, thin black line), and (e–h) temperature distributions observed from the transect survey on 11 September 2013. The blue (red) color in (b) indicates the onshore (offshore) flow. Shaded areas in (a) indicate transect observation periods: (A–D). The data shown in (c) and (d) were obtained at 2.5 m above the bottom (deeper site) and at 1 m above the bottom (shallower site). HAB represents height above the bottom.

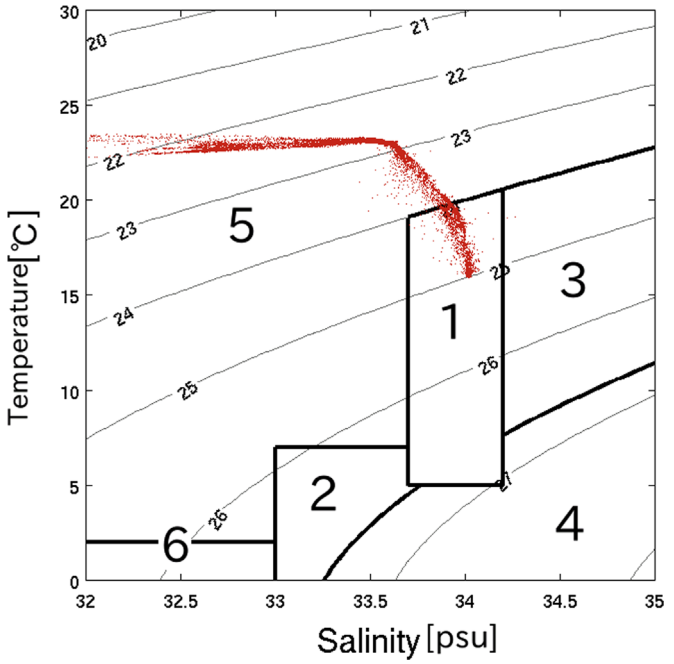

Fig. 8. Temperature–Salinity (TS) diagram for water observed in Otsuchi Bay and classification of six water systems from Hanawa and Mitsudera (1986). The six areas indicate water masses off the Sanriku Coast: 1. The Tsugaru Warm Current water system; 2. The Oyashio water system; 3. The Kuroshio water system; 4. The cold lower-layer system; 5. The surface water system; 6. The Coastal Oyashio water system.

in the deeper regions of the bay associated with internal bores (Fig. 6d and e). Masunaga et al. (2015) reported that current shear induced by internal bores contribute to vertical mixing of the river plume in Otsuchi Bay. Thus, river discharges do not influence the structure of internal bores, but the propagation of bores largely influences the surface river plume (Masunaga et al., 2015). The temperature–salinity (TS) diagram showed that the density in the cold water mass is controlled dominantly by temperature (Fig. 8). According to a study of water classification based on the TS relationship (Hanawa and Mitsudera, 1986), the low-temperature water mass in internal bores was identified as Tsugaru Warm Current water (Fig. 8). This water mass is derived from the northern region of the Sanriku Coast. Okazaki (1990) found the same water mass was observed in internal waves in Toni Bay, which is located near Otsuchi Bay.

3.2. Sediment resuspension

High turbidity water was observed at two locations: in the internal wave at depths of 20–40 m and in the shallow regions of the bay with depths of 5–15 m (Fig. 6f and g). The internal bore propagated along the slope accompanied by strong sediment resuspension at its head (Fig. 6g). In addition, sediment was suspended from the bed and entrained into the water column along the pycnocline. This feature is frequently observed over continental shelves and is called an intermediate nepheloid layer (INL, e.g., Thorpe, 1998; McPhee-Shaw, 2006). Strong sediment suspension was not observed before the cold-water intrusion period below 20 m depth. The turbidity data observed by the Compact-CTD mounted near the bottom (1 m above the bottom) at the mooring site showed burst-like sediment resuspension at the beginning of cold water intrusion periods, and high turbidity signals gradually decreased after the burst events (Fig. 4b). Unfortunately, the Compact-CTD power supply failed at 14:00 on 27 September. Therefore, turbidity data from the Compact-CTD were not obtained from the

last cold-water intrusion period (Event 3). Backscatter echo intensity data observed by the moored ADCP also show high echo intensity during cold-water intrusion periods (Fig. 4d).

The particle size distribution shows that the sediments consist of silts and sands below 15 m depth (Fig. 3, locations A and B) and near the river mouth (Fig. 3, location E). In contrast, sediments consist of only larger particles, such as sand, between depths of 5 m (Fig. 3, location D) and 11 m (Fig. 3, location C). A sandbar located at the Unosumai River mouth was completely eroded by the tsunami in March 2011, spreading sand into the interior of the bay (Okayasu et al., 2013). It is likely that the sandy area between 5 and 11 m depths is due to sand derived from the eroded sandbar. Therefore, internal bores propagating on the sloping bottom consist of a mixture of silts and sands.

3.3. Numerical results

Model results showed internal bores propagating into the bay and were in good agreement with the in situ observations (Fig. 9). When the bore wave propagated into the bay (surging period), the bore head was accompanied by a sharp cold front and a vortex (Fig. 9d and e; details of the vortex motion are described in the discussion). The horizontal flow field indicates onshore flow in the lower layer and offshore flow in the upper layer during the surging period (Fig. 9b, j and k), which is consistent with the field observations (Fig. 6i). The offshore currents in the bottom boundary layer shown in Fig. 9i were due to receding currents from the previous wave. During the receding phase, the currents switched direction and the cold bore propagated back offshore. In contrast to the receding cold water in the deeper area, the head of the bore continued to propagate into the shallows (Fig. 9l and m). The bore was strained along the sloping bottom by the downslope receding current and the upslope motion of the bore head during the receding phase. This straining led to a thinner bore in the vertical than during the surging period. The onshore flow was enhanced at the head of the bore (Fig. 9j–l). The maximum onshore flow appeared when the bore head passed through the initial thermocline depth (40 m), and the maximum speed reached 0.36 m s^{-1}. Above the thermocline, the onshore currents became slow as the bore propagated into shallow water (Fig. 9j–l).

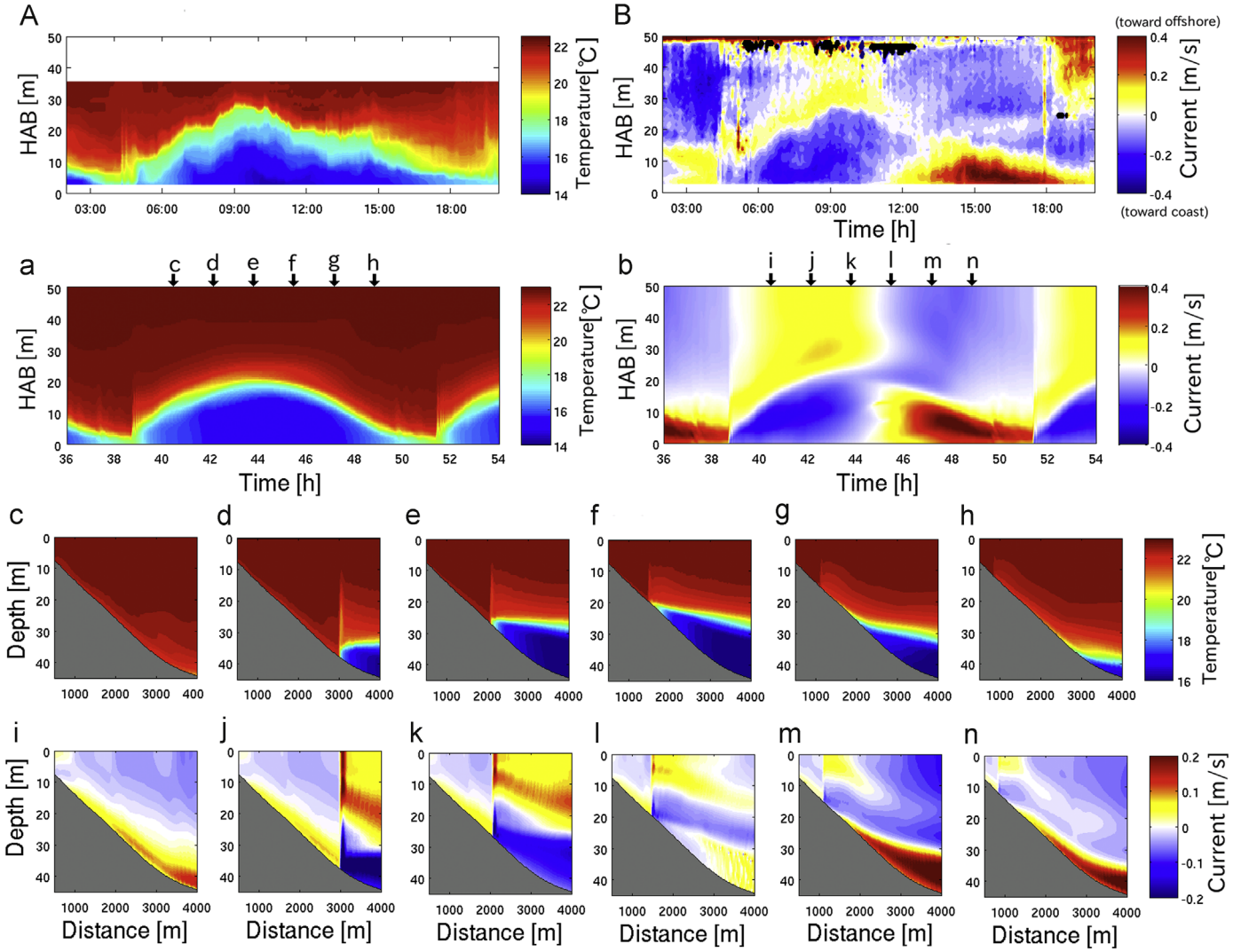

Fig. 9. (Color figure online). (A, B) Observed and (a–n) modeled results. Time series of (A) temperature and (B) east–west current from the moorings in September 2013. Time series of (a) temperature and (b) horizontal current at 50-m depth, and snapshots of (c–h) temperature distributions and (i and j) horizontal current distributions in the transect line from the numerical simulations. Arrows in teh upper *x* axis in panels (a) and (b) indicate the timing of snapshots shown in (c–n). The blue (red) color in panels (b) and (i–n) indicates onshore (offshore) flow. HAB represents height above the bottom.

4. Discussion

4.1. Vortex motion at the head of the bore

Internal bores accompanied by strong currents induce a vortex motion at their heads (Boegman and Ivey, 2009; Van Haren, 2009; Masunaga and Yamazaki, 2014). The vortex is derived from intensification of vorticity within the shoaling internal gravity wave due to localized straining by the shoreward flow along the bottom and the vertical ejection of flow at the head of the bore (Boegman and Ivey, 2009; Masunaga and Yamazaki, 2014). Van Haren (2009) observed the vortex structure accompanied by strong vertical resuspension of sediments that reached 40 m above the sloping bottom. In shallow areas, Richards et al. (2013) observed vortex packets accompanied by vertical sediment resuspension that reached 10 m above the bottom. One-minute averaged ADCP current data, observed during Event 3 (September 27, 2012), showed onshore flow (0.1 m s^{-1}) near the bottom, a strong upward ejection flow (0.02–0.03 m s^{-1}) at the head of the bore, and a downward flow in the lee of the bore head (Fig. 10a and b, Time 14:05–14:10). These motions indicated that the vortex motion was induced by the shoaling internal bore (a schematic image of the vortex is depicted in Fig. 10e). Venayagamoorthy and Fringer (2006) reported that internal waves with high Froude numbers ($Fr=u/c$ is the ratio of the current magnitude, u, to the internal wave speed, c) tend to generate highly nonlinear vortex motions along the slope. We estimated the Froude number by using observed bore propagation speed and current speed in the bore. In the case of event 3, the maximum flow speed in the bore was approximately 0.15 m s^{-1} and the propagation speed of the bore was roughly 0.14 m s^{-1}, consistent with highly nonlinear motions in high Froude number ($Fr\sim 1$) flows. Numerical simulation results also showed $Fr>1$ at the head of the bores during, reaching $Fr=1.3$. Consequently, enhanced bottom flows induced by internal bores were driven upward leading to the vortex motion. The echo intensity showed that suspended sediments follow a ring-like vortex motion and are lifted up to 8 m above the bottom (Fig. 10c). In addition, the temperature distribution showed the vortex structure and the upward motion at the head of the bore (Fig. 10d). The beginning of the bore event recorded by the ADCP was approximately 7 min ahead of that recorded by the thermistor array. This lag was due to the distance (120 m) between the two mooring sites (Fig. 1c). High-frequency ($\sim N$) upward and downward wave motions accompanied by isothermal depth displacements remained after the burst-like vortex event (Time=14:06–14:30). As we described earlier, these high-frequency motions in the lee of the vortex may be due to a shear instability (Antenucci and Imberger, 2001; Boegman et al., 2003).

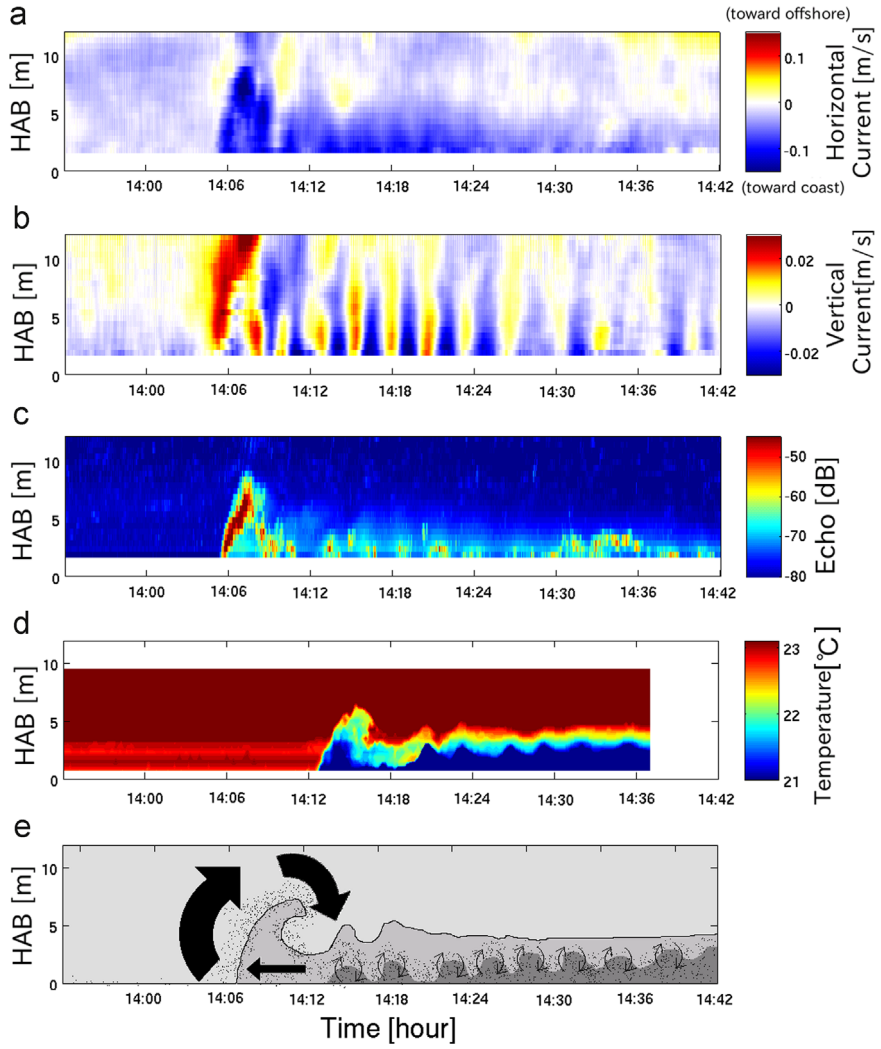

Fig. 10. (a) East–west currents [m s^{-1}], (b) vertical currents [m s^{-1}] and (c) echo intensity [dB] from the moored ADCP, and (d) temperature from the thermistor array during the bore wave period on 27 September 2012 (during Event 3). Panel (e) depicts a schematic of the vortex motion at the head of the bore wave. The time lag (approximately 7 min) between the ADCP data and the thermistor chain data is due to the distance of 120 m between the two mooring sites. HAB represents height above the bottom.

Although the high-resolution mooring data showed the vortex motion accompanied by strong currents and vertical sediment resuspension, the YODA Profiler observations did not capture the vortex structure (Fig. 6c). The horizontal scale of the vortex may be estimated from observed time scale of the vortex (360 s, Fig. 10) and the horizontal currents in the vortex (0.1 m s^{-1}, Fig. 10a), which suggests that the scale of the vortex is approximately 36 m. Since the precise propagation direction of the vortex in the horizontal is unknown and the propagation speed of the vortex is less than the average horizontal current speed (Hosegood et al., 2004), the actual vortex scale could be even less than 36 m. The horizontal resolution of the YODA Profiler observations was approximately 100 m near the head of the bore, which is too large to capture vortex structures at the head of the bore.

Numerical simulations reproduced the vortex motion at the head of the bore (Fig. 9 d, e, j and k). The horizontal flow speed is enhanced at the head of the bore and the maximum Froude number within the bore was approximately 1.3. In addition to the bottom flow, the vortex motion enhanced the opposite flow near the surface (Fig. 9j and k). The vortex core propagated along the slope with a similar structure to solitary waves advancing along bottom slopes (Klymak and Moum, 2003; Richards et al., 2013). The horizontal scale of the vortex resolved by numerical simulations is approximately 100 m (Figs. 9d and e and 11a). However, this scale was approximately three times larger than the scale (36 m) estimated from the observations. The large-scale vortex motion in the model was likely due to the limited resolution, since the horizontal grid spacing (Δx=20 m) was too large to capture such a small vortex motion.

To resolve the small vortex motion, we used a smaller domain with a higher grid resolution. The new domain had a length of 320 m and horizontal and vertical grid spacings of 0.64 m and 0.22 m, respectively. The finer resolution model was forced by a cold-water intrusion from the deeper boundary (0.1 m s^{-1}) and a weak outflow was set above the cold water intrusion layer to ensure zero net total volume flux. The shallower boundary was set as an open boundary. The smaller-domain model reproduces the fine features associated with the vortex motion (Fig. 11b and c). The horizontal scale of the vortex was approximately 20 m and was five times smaller than that from the coarser model. The vertical ejection current and the downward current at the head of the wave reached 0.03 m s^{-1}, which is consistent with the observed result shown in Fig. 10a and b. The time series of the vortex from the model was compared with the observed feature from the mooring survey (Fig. 11f and g) and showed a good agreement between the model and the observation. Although the model qualitatively reproduced the observed vortex motions, details of small-scale or turbulent-like motions in the vortex were not reproduced by the model (e.g., shear instability) because the Reynolds number in the model is significantly smaller than that in reality. The Reynolds number roughly estimated from the vertical scale of vortex and the current speed was an order of 10^5, which satisfies to generate strong turbulent motions.

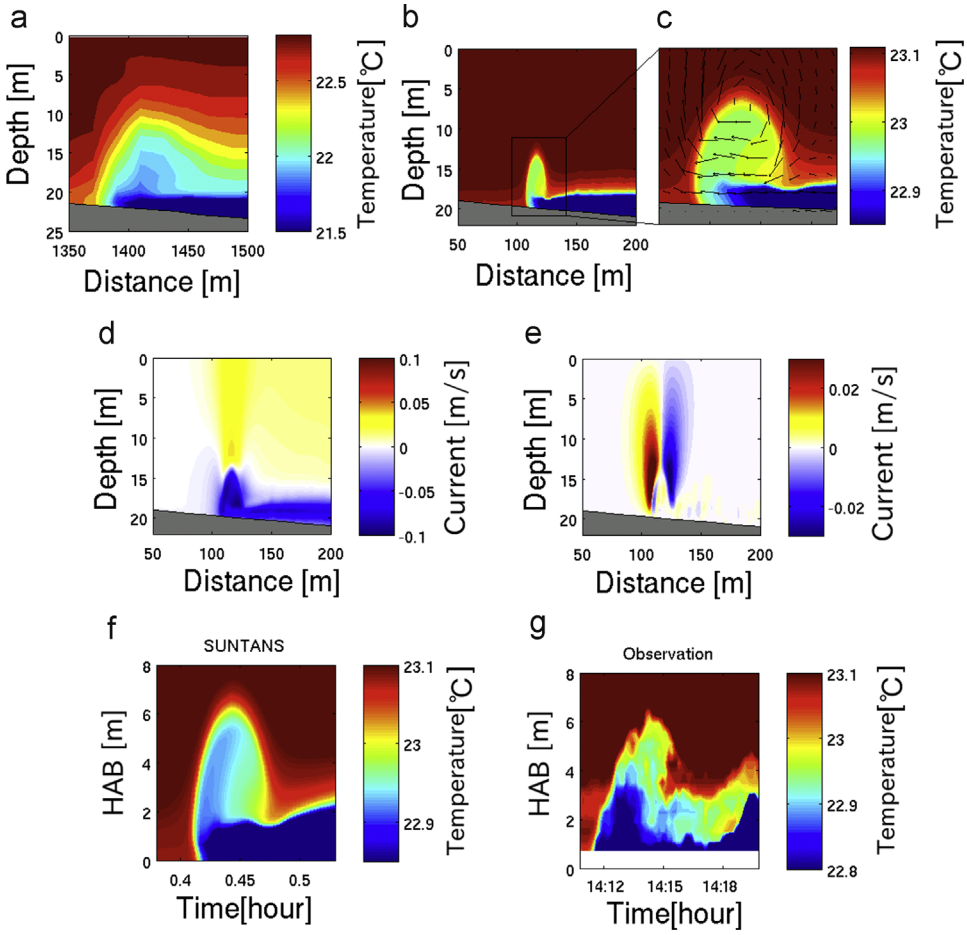

Fig. 11. Numerical results of temperature at the bore head from (a) the coarser and (b, c) the finer model runs. (d) Horizontal currents and (e) vertical currents from the finer model. Bottom two panels show time series of the temperature at the bore head from (f) the numerical model and (g) the observations. The range of the horizontal axes in panels (f) and (g) is the same. HAB represents height above the bottom.

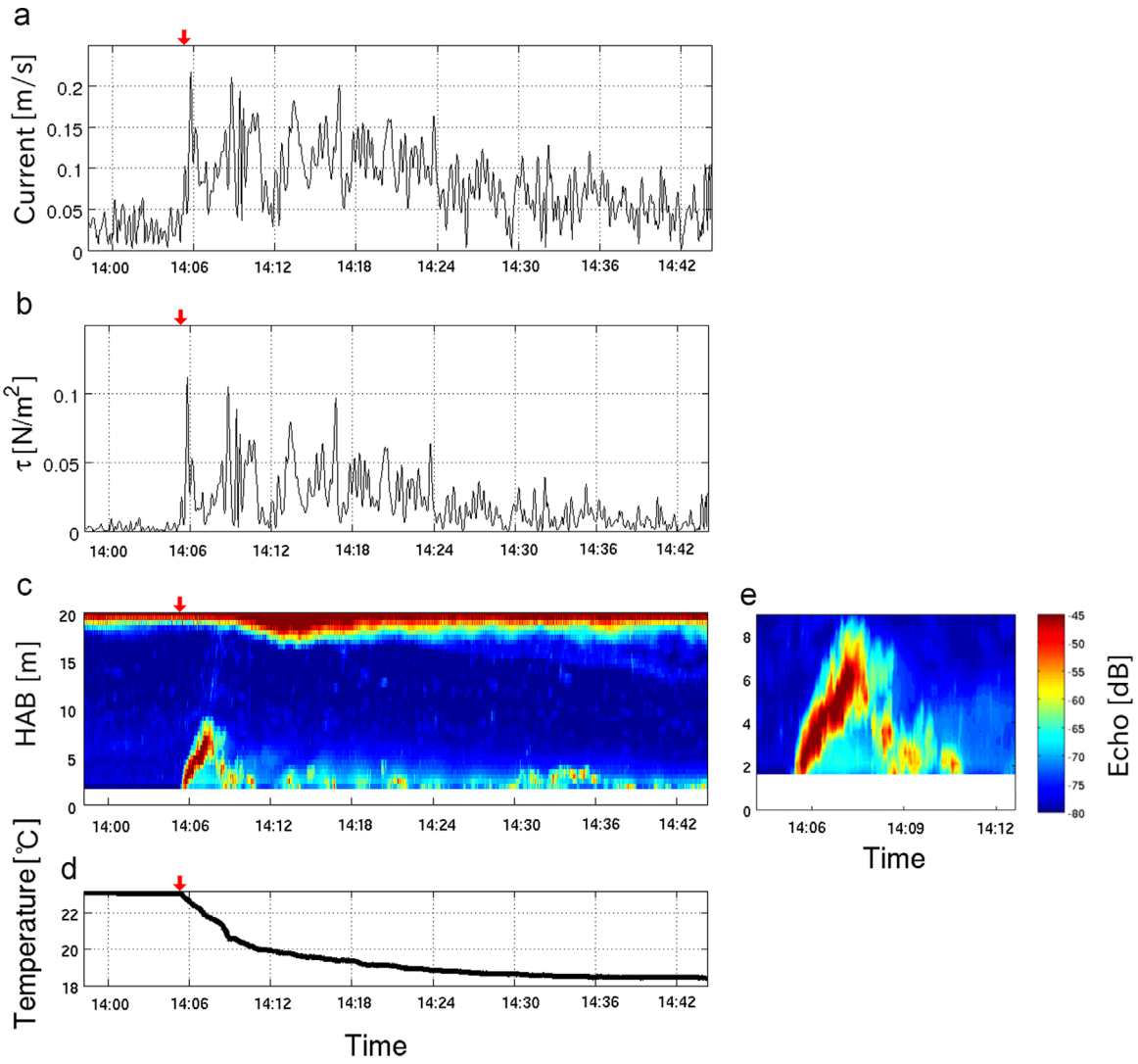

Fig. 12. (Color figure online). (a) Velocity due to the internal wave at 2 m above the bottom, (b) bottom shear stress τ N m^{-2}, (c, e) echo amplitude, and (d) temperature time series from the moored ADCP on 27 September 2012 (Event 3). Panel (e) is a close-up of the echo amplitude at the beginning of the bore wave period. Red arrows in panels (a–d) indicate the beginning of the internal bore wave period. HAB represents height above the bottom.

4.2. Sediment resuspension and bottom friction

In order to remove the sea surface gravity wave signal, the current data shown in Fig. 12 were low-pass filtered with a cutoff frequency at 0.05 Hz. Time series of near-bottom currents were weak (less than 0.06 m s^{-1}) before the bore period (Fig. 12a). On the other hand, the current was high when the cold water intrusion propagated across the observation site (Fig. 12a, Time > 14:06). The currents due to the internal wave reached 0.22 m s^{-1} during the first burst-like event (Fig. 12a). To determine whether the bed shear stress induced by the bore was sufficient to resuspend sediments, we estimated it with

$$\tau = \rho C_D U^2, \tag{4}$$

where $\rho = 1024$ kg m^{-3} is the water density, C_D is the drag coefficient and U is the current speed above the bottom. The drag coefficient is given by

$$C_D = \left[\frac{\kappa}{\ln(z/z_0)}\right]^2, \tag{5}$$

where $\kappa = 0.41$ is von Kármán constant, z is the height above the bottom and $z_0 = 5 \times 10^{-4}$ m is the bottom roughness (Quaresma et al., 2007). The bed shear stress, τ, estimated from the observed currents and Eq. (5) fluctuated significantly during the bore period between 0.05 and 0.11 N m^{-2} (Fig. 12b), although the average shear stress at the head of the bore was approximately 0.033 N m^{-2} between 14:06 and 14:12. Based on the sediment samples at a depth of 20 m that indicated the presence of silts (Fig. 3), the critical value of the bed shear stress for sediment resuspension by the bores is approximately 0.03–0.1 N m^{-2} (e.g., Gardner, 1989; Cacchione et al., 2002; Ross et al., 2009). Thus, the estimated shear stress due to the internal bore was sufficient to suspend sediments. Previous studies reported burst-like currents inducing resuspension above the sloping bottom (Gloor et al., 1994; Bonnin et al., 2006; Boegman and Ivey, 2009). The first burst-like strong current event coincided with strong sediment resuspension as revealed from the echo intensity (Fig. 12c).

According to Stokes' law, the terminal velocity of fine suspended particles is approximately 0.3–8 m h^{-1} (8.9×10^{-5}–2.2×10^{-3} m s^{-1}) when the particle size and density are 10–50 μm and 2.65 g cm^{-3} (typical value for wet silts), respectively. Because the terminal velocity of suspended particles (8.9×10^{-5}–2.2×10^{-3} m s^{-1}) is much lower than the upward motion in the vortex (Fig. 10b), suspended particles

can be lifted up to 8 m above the bottom within a few minutes by the vortex as shown in Fig. 12e. Furthermore, the displacement speed of the thermocline during bore run-up (1.4×10^{-3} m s^{-1}) was faster than the terminal velocity for fine sediments. These fine sediments are lifted up along the interface of the bore and are subsequently transported offshore by the reversing flow above the bore (Fig. 6f–i). During the receding phase of the internal tide, suspended particles have time to settle onto the bottom prior to arrival of the next internal tide. Consequently, no suspension is evident below 20 m prior to arrival of the bore (Fig. 6, period A).

The observed data from the mooring at the deeper site (54-m depth) in 2013 showed strong onshore currents near the bottom reaching 0.25 m s^{-1} and an associated bed shear stress reaching 0.15 N m^{-2} during the internal wave surging period (Fig. 7b). The current velocity and bed shear stress were higher during the receding phase than those during the run-up, and exceeded 0.4 m s^{-1} and 0.38 N m^{-2}, respectively. If sediments contain silts at the deeper site that are the same as those at the shallower site (Fig. 3, locations A and B), the strong shear stress due to the internal waves in the deeper site was sufficient to suspend sediments. The speed of the current due to the internal waves decreased with the decrease in the depth of the bottom, since the gravity decelerates the onshore ward flow speed. The shoreward current speed at the shallower site was approximately 3 times slower than that at the deeper site, 0.07 m s^{-1} (Fig. 7cd).

High turbidity water was also observed near the shore at depths of 5–10-m (Fig. 6fg). However, the sediments in shallow waters are primarily sands and are therefore too large (100–300 μm) to expect any resuspension by the local currents (Fig. 3, locations C and D). Instead, high turbidity in the shallows was probably due to fine sediments transported from the Unosumai River mouth located at the western end of the bay. Much of these fine sediments are deposited offshore in deeper waters by turbidity currents originating at the Unosumai and other River mouths in the bay (Wright and Nittrouer, 1995; Kineke et al., 1996).

4.3. Turbulent mixing in the internal bore

Breaking of internal waves induce strong turbulent mixing and sediment resuspension (e.g., Thorpe, 1998; Cacchione et al., 2002; McPhee-Shaw and Kunze, 2002). Richards et al. (2013) measured a high dissipation rate exceeding 10^{-5} W kg^{-1} in shoaling bores along a shallow slope. The pseudo-dissipation rate, ε_P, estimated from the YODA Profiler showed strong turbulent mixing in the internal bore (Fig. 13a and b), while the measured pseudo-dissipation rate below a depth of 15 m was low before the internal bore event ($\varepsilon_P < 10^{-9}$ W kg^{-1}). The high dissipation rate ($\varepsilon_P \sim 10^{-8}$–$10^{-7}$ W kg^{-1}) near the surface (0–10 m) during both periods (A) and (B) was likely due to the wind stress. Masunaga et al. (2015) describes the turbulent mixing near the sea surface in the bay in more detail. We can estimate the dissipation in the observed bores from the law of the wall theory (Dewey and Crawford, 1988), which gives

$$\varepsilon_{LOW} = \frac{C_D^{3/2} u^3}{kz}, \tag{6}$$

where z is the height above the bed and u is the velocity above the bottom. With an internal bore-induced current of u=0.2–0.3 m s^{-1} at a depth of z=0.2 m, $\varepsilon_{LOW} \sim 1.1 \times 10^{-6}$–$3.7 \times 10^{-6}$ W kg^{-1}, which is consistent with the YODA observations which reached 10^{-6} W kg^{-1} at the bore head on 27 September.

The high dissipation rate did not only appear at the head of the wave, but also appeared along an isopycnal interface (Fig. 13b). It has been suggested that mixed/mixing bottom boundary water detaches from the sloping bottom and spreads along isopyncals into the ocean interior (Armi, 1978; McPhee-Shaw, 2006). The boundary detachment leads to the generation of intermediate nepheloid layers along isopyncals and contributes to mixing of the ocean interior. To the authors' knowledge, these are the first observations that directly link waters with high dissipation and sediment resuspension to their breaking internal bores.

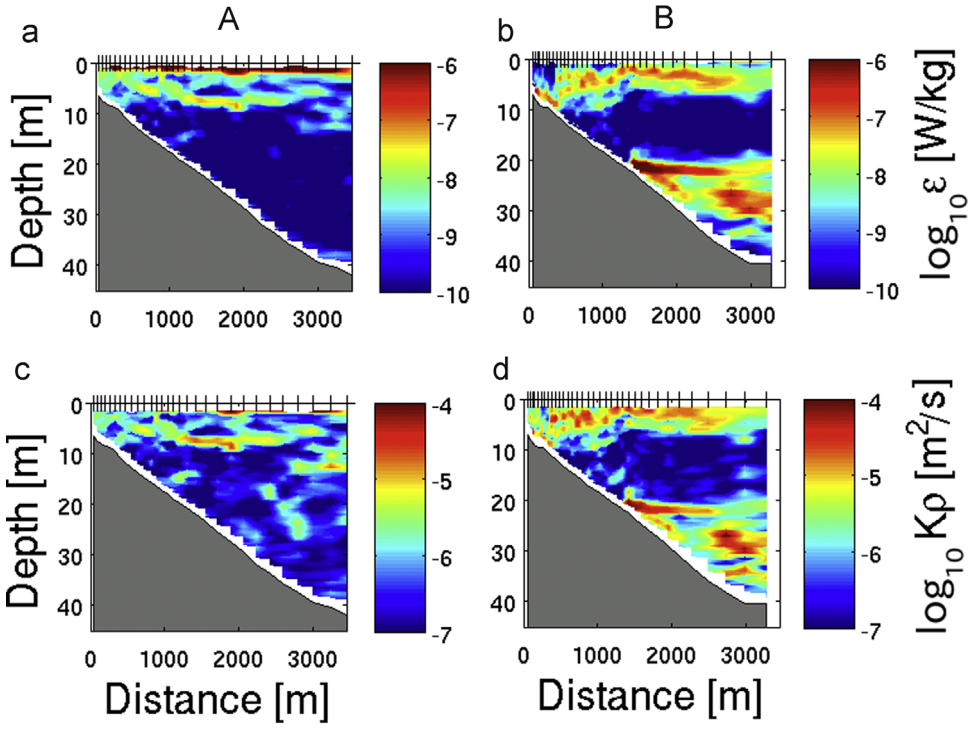

Fig. 13. (a, b) ε_P W kg^{-1} and (c, d) $K\rho$ m^2 s^{-1} distributions (a, c) before the bore wave period and (b, d) during the bore wave period estimated from the YODA Profiler observations on 27 September 2012 (Event 3).

The vertical turbulent diffusivity, $K\rho$, was estimated with (Osborn, 1980),

$$K_\rho = \gamma_{mix}\frac{\varepsilon}{N^2}, \tag{7}$$

where γ_{mix} is the efficiency factor (often referred as mixing efficiency). We selected a canonical efficiency factor $\gamma_{mix}=0.2$ (Osborn, 1980) to estimate the vertical eddy diffusivity from the YODA Profiler. The vertical turbulent diffusivity was high at the head of the bore wave and reached 10^{-4} m^2 s^{-1} (Fig. 13d). On the other hand, the background value of $K\rho$ was low at 10^{-7} m^2 s^{-1}, which is close to the molecular diffusivity of heat. Therefore, the internal bores play a significant role in mixing processes and turbulent heat fluxes in the bay. Recent studies suggested that the mixing efficiency is much higher than the 0.2 in the early stage of turbulent mixing and breaking of internal waves (e.g., Smyth et al., 2001). Although we could not estimate the true value of the mixing efficiency due to the lack of observational data, the vertical turbulent eddy-diffusivity at the head of the bore might be much higher than the results shown in Fig. 13d.

5. Conclusions

We observed fine features associated with breaking internal waves Otsuchi Bay using moored observations and the YODA Profiler. The YODA Profiler elucidated details of the run-up of internal bores on the slope in the bay. Distinct intermediate nepheloid layers were also observed and shown to be produced by the internal bores. Data from the high-resolution thermistor array revealed high-frequency motions ($\sim N$) in the lee of the bore wave that are likely induced by shear instability and the vortex structure at the head of the bore. Strong turbulent mixing was also observed in the bore, where the turbulent kinetic energy dissipation rate reached 10^{-6} W kg^{-1} at its head. A distinct propagating vortex at the head of the bore induced strong vertical velocities that reached 0.03 m s^{-1}. These upward currents transported sediments that had been suspended by the strong bottom currents in the bore into the vortex and produced a ring-like turbidity pattern as the sediments were entrained into the vortex.

The nonhydrostatic SUNTANS model reproduced the observed internal bores propagating into the bay. Consistent with the observations, the model results showed a thick bore front during the internal wave surging period followed by thin stretched downslope flow during the receding phase of the internal wave. Because the resolution of the domain for the bay-scale model was too coarse to reproduce the vortex motion, a smaller-scale domain was run with higher resolution that was able to reproduce the detailed structure of the vortex motion in the bore. Our study clearly indicates that internal bores generate locally intensified strong currents (a vortex) at the head of a shoaling internal wave that induce strong turbulent mixing and sediment resuspension.

Acknowledgments

We thank the crew of the R/V Grand-maillet (the University of Tokyo), the fishing boat Senshu-maru (Shin-Otsuchi Fishery), and the fishing boat Daimutsu-maru (Shin-Otsuchi Fishery) for their time and help. The authors gratefully acknowledge Kiyoshi Tanaka, Yuichiro Nishibe, and Yuka Saito for coordinating our observation plans. We are indebted to the laboratory members for their assistance with the deployment of the instruments. We also thank Lynn Allmon for her editorial assistance during the final preparation of the manuscript. This study was supported by funding from Tohoku Ecosystem-Associated Marine Science (TEAMS), a research program launched by the Ministry of Education, Culture, Sports, Science and Technology (MEXT).

References

Anbo, A., Otobe, H., Takagi, M., 2005. On the river water discharged into Otsuchi Bay. Rep. Int. Coast. Mar. Res. Cent. 30, 4–8.
Antenucci, J.P., Imberger, J., 2001. On internal waves near the high-frequency limit in an enclosed basin. J. Geophys. Res.: Oceans 106 (C10), 22465–22474.
Armi, L., 1978. Some evidence for boundary mixing in the deep ocean. J. Geophys. Res. 83, 1971–1979.
Boegman, L., Imberger, J., Ivey, G.N., Antenucci, J.P., 2003. High-frequency internal waves in large stratified lakes. Limnol. Oceanogr. 48 (2), 895–919.
Boegman, L., Ivey, G.N., 2009. Flow separation and resuspension beneath shoaling nonlinear internal waves. J. Geophys. Res.: Oceans 114, C02018.
Bonnin, J., van Haren, H., Hosegood, P., Brummer, G.J.A., 2006. Burst resuspension of seabed material at the foot of the continental slope in the Rockall Channel. Mar. Geol. 226, 167–184.
Bourgault, D., Blokhina, M.D., Mirshak, R., Kelley, D.E., 2007. Evolution of a shoaling internal solitary wavetrain. Geophys. Res. Lett. 34, L03601. http://dx.doi.org/10.1029/2006GL028462.
Broenkow, W.W., McKain, S.J., 1972. Tidal oscillations at the head of Monterey Submarine Canyon and their relation to oceanographic sampling and the circulation of water in Monterey Bay. Annual report, Part 6, September 1972. Moss Landing Marine Laboratories Technical Publication, California, p. 42 72-5.
Cacchione, D.A., Pratson, L.F., Ogston, A.S., 2002. The shaping of continental slopes by internal tides. Science 296, 724–727.
Carter, G.S., Gregg, M.C., Lien, R.C., 2005. Internal waves, solitary-like waves, and mixing on the Monterey Bay shelf. Cont. Shelf Res. 25, 1499–1520.
Dewey, R.K., Crawford, W.R., 1988. Bottom stress estimates from vertical dissipation rate profiles on the continental shelf. J. Phys. Oceanogr. 18, 1167–1177.
Dickson, R.R., McCave, I.N., 1986. Nepheloid layers on the continental slope west of Porcupine bank. Deep Sea Res. Part A 33, 791–818.
Foloni-Neto, H., Lueck, R., Mabuchi, Y., Nakamura, H., Arima, M., Yamazaki, H., 2014. A new quasi-horizontal glider to measure biophysical microstructure. J. Atmos. Ocean. Technol. 31, 2278–2293.
Fringer, O.B., Gerritsen, M., Street, R.L., 2006. An unstructured-grid, finite-volume, nonhydrostatic, parallel coastal ocean simulator. Ocean Model. 14, 139–173.
Fu, L.L., Holt, B., NASA, 1982. Seasat Views Oceans and Sea Ice with Synthetic-Aperture Radar. JPL Publication, California, pp. 81–120.
Gardner, W.D., 1989. Periodic resuspension in Baltimore Canyon by focusing of internal waves. J. Geophys. Res. 94, 18185–18194.
Gloor, M., Wüest, A., Münnich, M., 1994. Benthic boundary mixing and resuspension induced by internal seiches. Hydrobiologia 284, 59–68.
Hanawa, K., Mitsudera, H., 1986. Variation of water system distribution in the Sanriku coastal area. J. Oceanogr. Soc. Jpn. 42, 435–446.
Helfrich, K.R., 1992. Internal solitary wave breaking and run-up on a uniform slope. J. Fluid Mech. 243, 133–154.
Helfrich, K.R., Melville, W.K., 2006. Long nonlinear internal waves. Annu. Rev. Fluid Mech. 38, 395–425.
Hosegood, P., Bonnin, J., van Haren, H., 2004. Solibore-induced sediment resuspension in the Faeroe–Shetland channel. Geophys. Res. Lett. 31, L09301.
Huthnance, J.M., 1989. Internal tides and waves near the continental shelf edge. Geophys. Astrophys. Fluid Dyn. 48, 81–106.
Ivey, G.N., Winters, K.B., De Silva, I.P.D., 2000. Turbulent mixing in a sloping benthic boundary layer energized by internal waves. J. Fluid Mech. 418, 59–76.
Kineke, G.C., Sternberg, R.W., Trowbridge, J.H., Geyer, W.R., 1996. Fluid-mud processes on the Amazon continental shelf. Cont. Shelf Res. 16, 667–696.
Klymak, J.M., Moum, J.N., 2003. Internal solitary waves of elevation advancing on a shoaling shelf. Geophys. Res. Lett. 30, 31–34.
Leichter, J.J., Wing, S.R., Miller, S.L., Denny, M.W., 1996. Pulsed delivery of subthermocline water to Conch Reef (Florida Keys) by internal tidal bores. Limnol. Oceanogr. 41 (7), 1490–1501.
Masunaga, E., Yamazaki, H., 2014. A new tow-yo instrument to observe high-resolution coastal phenomena. J. Mar. Syst. 129, 425–436.
Masunaga, E., Fringer, O., Yamazaki, H., 2015. An observational and numerical study of river plume dynamics in Otsuchi Bay, Japan. J. Oceanogr. http://dx.doi.org/10.1007/s10872-015-0324-2
McPhee-Shaw, E.E., Kunze, E., 2002. Boundary layer intrusions from a sloping bottom: a mechanism for generating intermediate nepheloid layers. J. Geophys. Res.: Oceans 107, 3-1–3-16.
McPhee-Shaw, E.E., Sternberg, R.W., Mullenbach, B., Ogston, A.S., 2004. Observations of intermediate nepheloid layers on the northern California continental margin. Cont. Shelf Res. 24 (6), 693–720.
McPhee-Shaw, E.E., 2006. Boundary–interior exchange: reviewing the idea that internal-wave mixing enhances lateral dispersal near continental margins. Deep Sea Res. Part II: Top. Stud. Oceanogr. 53 (1), 42–59.
Mellor, G.L., Yamada, T., 1982. Development of a turbulence closure model for geophysical fluid problems. Rev. Geophys. 20 (4), 851–875.
Nakatsuka, T., Toda, M., Kawamura, K., Wakatsuchi, M., 2004. Dissolved and particulate organic carbon in the Sea of Okhotsk: transport from continental shelf to ocean interior. J. Geophys. Res.: Oceans 109, C09S14. http://dx.doi.org/10.1029/2003JC001909.

Nam, S., Send, U., 2011. Direct evidence of deep water intrusions onto the continental shelf via surging internal tides. J. Geophys. Res.: Oceans 116 (C5), C05004.
Okayasu, A., Shimozono, T., Yamazaki, H., Nagai, T., Sato, S., 2013. Severe erosion of sandbar at Unosumai River mouth, Iwate, due to 2011 Tohoku tsunami. Coast. Dyn. 2013, 1311–1320.
Okazaki, M., 1990. Internal tidal waves and internal long period waves in the Sanriku coastal seas, eastern coast of northern Japan. La mer 28, 5–29.
Okazaki, M., 1994. The circulation of sea water and variation of the properties in some bays of Sanriku Coast, eastern coast of Northern Japan. Bull. Coast. Oceanogr. 32, 15–28.
Osborn, T.R., 1980. Estimates of the local rate of vertical diffusion from dissipation measurements. J. Phys. Oceanogr. 10, 83–89.
Otobe, H., Onishi, H., Inada, M., Michida, Y., Terazaki, M., 2009. Estimation of water circulation in Otsuchi Bay, Japan inferred from ADCP observation. Coast. Mar. Sci. 33 (1), 78–86.
Petruncio, E.T., Rosenfeld, L.K., Paduan, J.D., 1998. Observations of the internal tide in Monterey Canyon. J. Phys. Oceanogr. 28, 1873–1903.
Pineda, J., 1994. Internal tidal bores in the nearshore: warm-water fronts, seaward gravity currents and the onshore transport of neustonic larvae. J. Mar. Res. 52 (3), 427–458.
Puig, P., Palanques, A., Guillén, J., El Khatab, M., 2004. Role of internal waves in the generation of nepheloid layers on the northwestern Alboran slope: implications for continental margin shaping. J. Geophys. Res.: Oceans 109, C09011. http://dx.doi.org/10.1029/2004JC002394.
Quaresma, L.S., Vitorino, J., Oliveira, A., da Silva, J., 2007. Evidence of sediment resuspension by nonlinear internal waves on the western Portuguese mid-shelf. Mar. Geol. 246 (2), 123–143.
Richards, C., Bourgault, D., Galbraith, P.S., Hay, A., Kelley, D.E., 2013. Measurements of shoaling internal waves and turbulence in an estuary. J. Geophys. Res.: Oceans 118 (1), 273–286.
Ross, C.B., Gardner, W.D., Richardson, M.J., Asper, V.L., 2009. Currents and sediment transport in the Mississippi Canyon and effects of Hurricane Georges. Cont. Shelf Res. 29 (11), 1384–1396.
Shea, R.E., Broenkow, W.W., 1982. The role of internal tides in the nutrient enrichment of Monterey Bay, California. Estuar. Coast. Shelf Sci. 15, 57–66.
Smyth, W.D., Moum, J.N., Caldwell, D.R., 2001. The efficiency of mixing in turbulent patches: inferences from direct simulations and microstructure observations. J. Phys. Oceanogr. 31 (8), 1969–1992.
Thorpe, S.A., 1998. Some dynamical effects of internal waves and the sloping sides of lakes, physical processes in lakes and oceans. Coast. Estuar. Stud. 54, 441–460.
Van Gastel, P., Ivey, G.N., Meuleners, M.J., Antenucci, J.P., Fringer, O., 2009. The variability of the large-amplitude internal wave field on the Australian North West Shelf. Cont. Shelf Res. 29 (11), 1373–1383.
Van Haren, H., 2009. Using high sampling-rate ADCP for observing vigorous processes above sloping (deep) ocean bottoms. J. Mar. Syst. 77, 418–427.
Van Weering, T.C.E., De Stigter, H.C., Balzer, W., Epping, E.H.G., Graf, G., Hall, I.R., Vangriesheim, A., 2001. Benthic dynamics and carbon fluxes on the NW European continental margin. Deep Sea Res. Part II: Top. Stud. Oceanogr. 48 (14), 3191–3221.
Venayagamoorthy, S.K., Fringer, O.B., 2006. Numerical simulations of the interaction of internal waves with a shelf break. Physics of Fluids 18, 076603. http://dx.doi.org/10.1063/1.2221863 076603/9.
Vlasenko, V., Hutter, K., 2002. Numerical experiments on the breaking of solitary internal waves over a slope–shelf topography. J. Phys. Oceanogr. 32, 1779–1793.
Vlasenko, V., Stashchuk, N., Hutter, K., 2005. Baroclinic Tides: Theoretical Modeling and Observational Evidence. Cambridge University Press, Cambridge, UK.
Vlasenko, V., Guo, C., Stashchuk, N., 2012. On the mechanism of A-type and B-type internal solitary wave generation in the northern South China Sea. Deep Sea Res. Part I: Oceanogr. Res. Pap. 69, 100–112.
Wallace, B.C., Wilkinson, D.L., 1988. Run-up of internal waves on a gentle slope in a two-layered system. J. Fluid Mech. 191, 419–442.
Walter, R.K., Woodson, C.B., Arthur, R.S., Fringer, O.B., Monismith, S.G., 2012. Nearshore internal bores and turbulent mixing in southern Monterey Bay. J. Geophys. Res.: Oceans 117 (C7), C07017.
Wang, Y.H., Lee, I.H., Liu, J.T., 2008. Observation of internal tidal currents in the Kaoping Canyon off southwestern Taiwan. Estuar. Coast. Shelf Sci. 80 (1), 153–160.
Wright, L.D., Nittrouer, C.A., 1995. Dispersal of river sediments in coastal seas: six contrasting cases. Estuaries 18 (3), 494–508.